Journal of Science and Transport Technology
Journal homepage: https://jstt.vn/index.php/en

UNIVERSITY OF TRANSPORT TECHNOLOGY

Article info
Type of article:
Original research paper

DOI:
https://doi.org/10.58845/jstt.utt.2026.en.6.4.177-193

***Corresponding author:**
Email address:
hungvt@utt.edu.vn

Received: 30/03/2026
Received in Revised Form: 19/06/2026
Accepted: 26/06/2026

Thermal buckling and postbuckling analysis of FG-CNTRC cylindrical shells stiffened by helical FG-CNTRC stiffeners with temperature-dependent material properties

Le Kha Hoa[1], Vu Tho Hung[2,*], Vu Minh Duc[3,4]
[1]Faculty of Fundamental Science, Military Academy of Logistics, Hanoi, Vietnam
[2]Mechanics of Advanced Materials and Structures, University of Transport Technology, Hanoi, Vietnam
[3]Mechanics of Advanced Materials and Structures, Institute for Advanced Study in Technology, Ton Duc Thang University, Ho Chi Minh City, Vietnam
[4]Faculty of Civil Engineering, Ton Duc Thang University, Ho Chi Minh City, Vietnam

Abstract: This study presents an analytical investigation on the thermal buckling and postbuckling behavior of functionally graded carbon nanotube-reinforced composite (FG-CNTRC) cylindrical shells reinforced by FG-CNTRC stiffeners. The shell is subjected to a uniform temperature rise, and the material properties of both the shell and stiffeners are assumed to be temperature-dependent. Three stiffening configurations, including orthogonal and helical stiffeners, are considered within a unified formulation based on the smeared stiffener technique. The governing nonlinear equilibrium equations are established using the Donnell shell theory with von Kármán geometric nonlinearity. A Ritz-based energy approach is employed to derive the analytical expressions for the critical buckling temperature and postbuckling equilibrium paths. The effects of CNT distribution patterns, CNT volume fraction, stiffener configuration, and geometric parameters on the thermal stability of the shells are systematically examined. The results indicate that stiffeners significantly enhance the thermal buckling resistance of FG-CNTRC cylindrical shells, with helical stiffeners providing a markedly higher improvement compared to orthogonal stiffeners. Among the considered CNT volume fractions, an intermediate value provides the highest thermal buckling resistance, while a further increase in CNT content may reduce the thermal stability. In addition, the spacing and arrangement of stiffeners play a crucial role in determining the buckling temperature and postbuckling response.

Keywords: FG-CNTRC cylindrical shell, Thermal buckling, Postbuckling behavior, FG-CNTRC stiffeners, Ritz method, Temperature-dependent material properties.

1. Introduction

In recent decades, cylindrical shells and other shell structures of revolution fabricated from advanced composite materials have attracted considerable attention due to their widespread applications in aerospace, marine, and mechanical engineering systems. Their superior strength-to-weight ratio and tunable material properties make them particularly suitable for high-performance structural components, thereby motivating extensive research into their mechanical behavior.

Functionally graded materials (FGMs) represent a class of advanced composites characterized by the continuous variation of their thermo-mechanical properties through the thickness of the structure. This gradual transition in material composition effectively reduces stress concentrations and enhances structural performance under complex loading conditions. Owing to these advantageous features, the thermo-mechanical behavior of FGM plates and shells has been extensively investigated over the past decade. A considerable number of studies have been devoted to the analysis of FGM cylindrical shells under various loading and environmental conditions. For instance, Sofiyev and Schnack [1] investigated the linear torsional dynamic buckling of FGM cylindrical shells subjected to time-dependent torsion using a Galerkin-based approach, neglecting inertia effects in the longitudinal and circumferential directions. Subsequent works by Sofiyev and co-authors [2, 3] further examined the torsional vibration characteristics and linear buckling behavior of FGM cylindrical shells and shells with FGM coatings, including the influence of Pasternak-type elastic foundations. The thermal stability of FGM shells has also been widely explored. Bagherizadeh et al. [4] analyzed the linear thermal buckling behavior of FGM cylindrical shells considering foundation effects, while Han et al. [5], based on Flügge shell theory, evaluated the vibration response and critical loads under internal pressure. In addition, Wang et al. [6] studied the influence of temperature distribution and porosity patterns on the vibration characteristics of FGM cylindrical shells, highlighting the importance of material inhomogeneity. Nonlinear thermo-mechanical responses have attracted increasing attention in recent years. Javani et al. [7] employed a hybrid numerical scheme combining the generalized differential quadrature method and Crank-Nicolson technique to investigate axisymmetric FGM conical shells under rapid thermal loading. Xu et al. [8] proposed a material design involving carbon fiber-reinforced polymers with FGM coatings for cylindrical shells. Furthermore, Arazm et al. [9] examined the dynamic behavior of axially symmetric FGM cylindrical shells subjected to moving loads using an analytical formulation. More recently, the incorporation of stiffeners into FGM shells has been considered to enhance structural performance. By extending the classical smeared stiffener technique, Nam et al. [10, 11] and Phuong et al. [12] developed governing equations for multilayer and sandwich FGM cylindrical shells reinforced with isotropic and FGM stiffeners, including ring, stringer, and helical configurations, while accounting for thermal effects and foundation interactions. Their studies addressed both linear and nonlinear buckling responses under torsional loading, covering prebuckling, bifurcation, and postbuckling regimes.

Carbon nanotubes (CNTs), since their discovery, have attracted significant attention due to their exceptional mechanical, thermal, and electrical properties. As a nanoscale reinforcement, CNTs have been widely incorporated into conventional matrix materials to remarkably enhance stiffness, strength, and thermal resistance. Building upon the concept of functionally graded materials, functionally graded carbon nanotube-reinforced composites (FG-CNTRCs) have been developed, in which the CNT volume fraction varies continuously through the thickness of the structure [13-15]. Owing to their superior performance, FG-CNTRCs have demonstrated considerable potential in improving the thermo-mechanical behavior of cylindrical shells and other shell structures, including toroidal segments.

Extensive efforts have also been devoted to the analysis of FG-CNTRC cylindrical shells under various mechanical and thermal loading conditions. In particular, buckling and postbuckling responses under axial compression, external pressure, and torsional loading have been investigated using advanced analytical approaches such as the two-step perturbation technique in conjunction with nonlinear higher-order shear deformation theories [13-16], with consideration of uniform temperature rise. The dynamic behavior of FG-CNTRC shells has likewise been widely explored. Free and forced vibration characteristics have been examined through energy-based formulations, including the Ritz method with Chebyshev polynomials and the variational differential quadrature method [16, 17]. Beyond cylindrical configurations, other shell structures such as truncated conical shells have also been analyzed using FG-CNTRC materials under various loading scenarios [18, 19]. In addition, recent studies have focused on enhancing the structural performance of FG-CNTRC shells through advanced design concepts. These include the incorporation of auxetic cores and the introduction of different stiffening schemes, such as ring, stringer, and helical stiffeners, with the nonlinear postbuckling behavior typically analyzed using Galerkin-based formulations [20-22]. Furthermore, the complex response of FG-CNTRC cylindrical shells under multi-physical environments, including seismic excitation combined with thermal and moisture effects, has been investigated using Ritz-type energy methods [23]. Particular attention has been given to the thermal stability of FG-CNTRC cylindrical shells with temperature-dependent material properties. In this context, Shen [24] and Hieu and Tung [25] examined the thermal buckling and postbuckling behavior using perturbation techniques and Galerkin methods, respectively, providing important insights into the nonlinear response of such structures.

Despite the extensive body of research on FGM and FG-CNTRC cylindrical shells, most existing studies have primarily focused on unstiffened shells or shells reinforced by conventional stiffening configurations. Although several works have considered stiffened FGM or FG-CNTRC shells, the combined effects of advanced stiffening schemes, such as orthogonal and helical stiffeners, together with temperature-dependent material properties, have not been comprehensively clarified. In particular, a unified analytical formulation that enables a consistent comparison between different stiffener configurations under thermal loading remains limited. Moreover, previous investigations have predominantly employed perturbation or Galerkin-based approaches, while Ritz-based energy formulations for such complex stiffened FG-CNTRC shell systems are still relatively scarce in the literature. This limitation motivates the development of an alternative analytical framework capable of capturing both buckling and postbuckling responses with improved flexibility in assumed displacement fields.

Therefore, the present study aims to develop a Ritz-based analytical model for investigating the thermal buckling and postbuckling behavior of FG-CNTRC cylindrical shells reinforced by FG-CNTRC stiffeners. Both orthogonal and helical stiffener configurations are considered within a unified framework, and the effects of CNT distribution patterns, stiffener arrangement, and geometric parameters on the thermal stability of the shells are systematically examined.

2. FG-CNTRC cylindrical shell model with FG-CNTRC stiffeners

Consider a FG-CNTRC cylindrical shell reinforced by stiffeners and subjected to a uniform temperature rise ΔT. The shell geometry is characterized by the circumferential radius R, thickness h, longitudinal radius a, and length L, as illustrated in Fig. 1. A cylindrical coordinate system $Oxyz$ is defined such that the origin is located on the mid-surface at the shell edge. The Ox-axis is aligned with the meridional direction, the Oy-axis follows the circumferential direction, and the Oz-axis is directed radially outward.

The shell is reinforced by three types of stiffeners, namely longitudinal, circumferential, and helical stiffeners. The geometric parameters of the stiffeners, including height, width, and spacing, are denoted by h_{st}, h_{ri}, h_{sp}, b_{st}, b_{ri}, b_{sp}, and d_{st}, d_{ri}, d_{sp}, respectively. For the sake of simplicity, these parameters are assumed to be identical in the present analysis, i.e., $h_{st} = h_{rt} = h_{sp} = h_s$, $b_{st} = b_{ri} = b_{sp} = b_s$ and $d_{st} = d_{ri} = d_{sp} = d_s$.

The inclination angle δ of the helical stiffeners with respect to the Ox-axis is related to the number of stiffeners n_{sp} and their spacing d_{sp} through the following expression [10-12]

$$\delta = \arccos\left(\frac{n_{sp} d_{sp}}{2\pi R}\right)$$

The volume fraction of CNTs across the panel thickness $(-h/2 \le z \le h/2)$ is assumed to follow either a uniform or a linear distribution, expressed as follows

$$\hat{V}_{CNT} = \begin{cases} V^*_{CNT} & (UD) \\ \dfrac{4V^*_{CNT}|z|}{h} & (X) \\ 2V^*_{CNT} - \dfrac{4V^*_{CNT}|z|}{h} & (O) \end{cases} \quad (1)$$

and for stiffeners $(h/2 \le z \le h/2 + h_{st})$

$$\hat{V}_{CNT} = \begin{cases} V^*_{CNT} & (UD) \\ \left|(2h - 4z)V^*_{CNT}/h_{st} + 2V^*_{CNT}\right| & (X) \\ 2V^*_{CNT} - \left|\begin{matrix}(4z - 2h)V^*_{CNT}/h_{st} \\ -2V^*_{CNT}\end{matrix}\right| & (O) \end{cases} \quad (2)$$

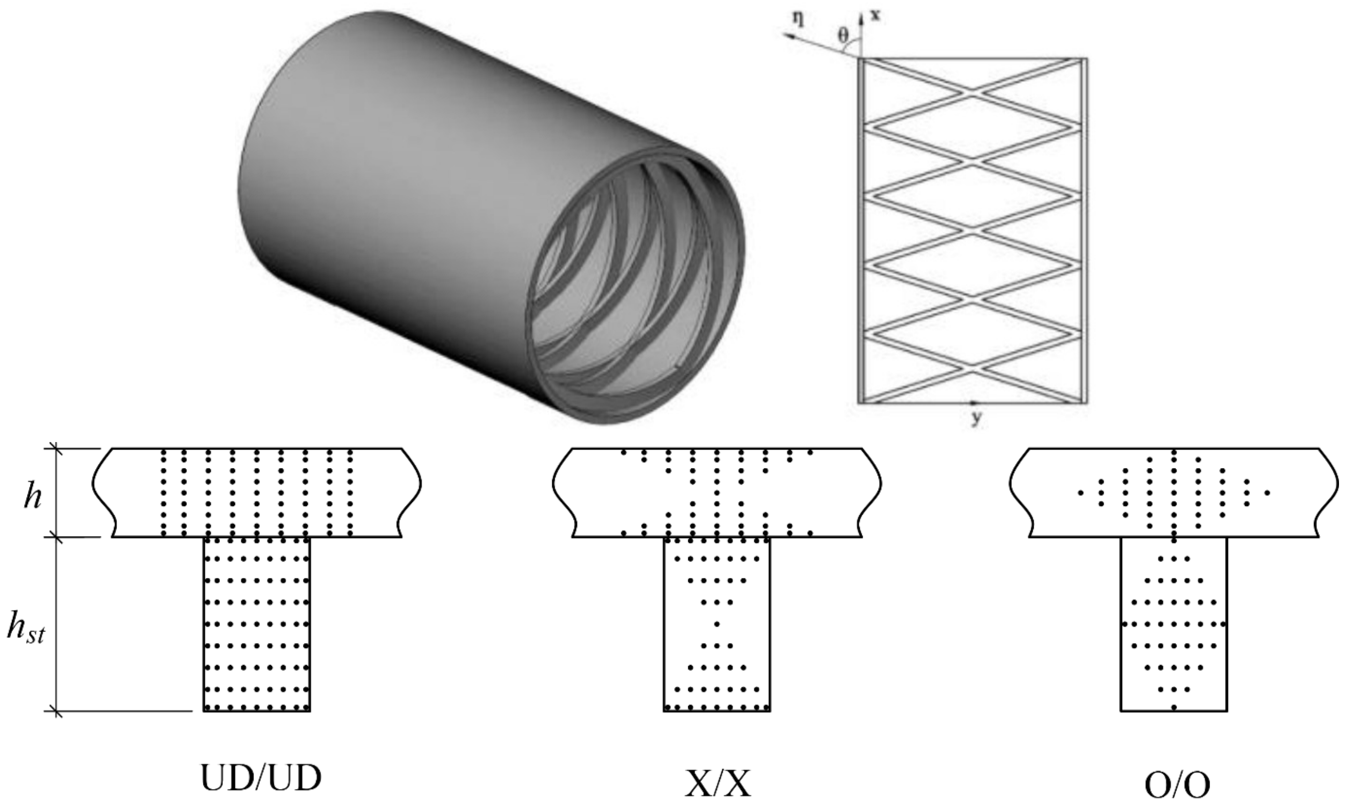

Fig. 1. Geometry of FG-CNTRC cylindrical shell reinforced by helical stiffeners and schematic illustration of CNT distribution patterns in the shell and stiffeners

Both the shell and the stiffeners are characterized by specific CNT distribution patterns, including UD/UD, X/X, and O/O configurations.

The effective elastic properties of the FG-CNTRC material are evaluated using the extended rule of mixtures. Accordingly, the expressions for Young's moduli, shear moduli, and Poisson's ratio can be formulated as follows [13-15]

$$\hat{E}_{11}^{CNT} = \hat{\eta}_1^{CNT}\hat{V}_{CNT}\hat{E}_{11}^{CN} + \hat{V}_M\hat{E}_M,$$
$$\frac{\hat{\eta}_2^{CNT}}{\hat{E}_{22}^{CNT}} = \frac{\hat{V}_{CNT}\hat{E}_M + \hat{V}_M\hat{E}_{22}^{CN}}{\hat{E}_{22}^{CN}\hat{E}_M},$$
$$\frac{\hat{\eta}_3^{CNT}}{\hat{G}_{12}^{CNT}} = \frac{\hat{V}_{CNT}\hat{G}_M + \hat{V}_M\hat{G}_{12}^{CN}}{\hat{G}_{12}^{CN}\hat{G}_M}, \tag{3}$$
$$\hat{\nu}_{12}^{CNT} = V_{CNT}^{*}\hat{\nu}_{12}^{CN} + \hat{V}_M\hat{\nu}_M.$$

where the effective material properties are defined based on the volume fractions of the constituents, in which $\hat{V}_{CNT}$ and $\hat{V}_M$ represent the CNTs and matrix phases, respectively, with the constraint $\hat{V}_{CNT} + \hat{V}_M = 1$. The mechanical properties of the CNTs are characterized by the elastic constants $\hat{E}_{11}^{CN}$, $\hat{E}_{22}^{CN}$, and $\hat{G}_{12}^{CN}$, whereas those of the isotropic matrix are given by $\hat{E}_M$ and $\hat{G}_M$. To account for nanoscale effects, the efficiency parameters $\eta_j^{CNT}\,(j = 1,\ 2,\ 3)$ are introduced based on numerical simulations. In addition, the Poisson's ratios corresponding to the CNTs and the matrix are denoted by $\hat{\nu}_{12}^{CN}$ and $\hat{\nu}_M$, respectively.

The thermal expansion behavior of both the shell and stiffeners along the x- and y-directions is characterized by the following coefficients

$$\hat{\alpha}_{11}^{CNT} = \frac{\hat{V}_{CNT}\hat{E}_{11}^{CN}\hat{\alpha}_{11}^{CN} + \hat{V}_M\hat{E}_M\hat{\alpha}_M}{\hat{V}_{CNT}\hat{E}_{11}^{CN} + \hat{V}_M\hat{E}_M},$$
$$\hat{\alpha}_{22}^{CNT} = \left(1+\hat{\nu}_{12}^{CN}\right)\hat{V}_{CNT}\hat{\alpha}_{22}^{CN} + \tag{4}$$
$$\left(1+\hat{\nu}_M\right)\hat{V}_m\hat{\alpha}_M - \hat{\nu}_{12}^{CNT}\hat{\alpha}_{11}^{CNT}.$$

where the coefficients of thermal expansion associated with the CNTs and the isotropic matrix are represented by $\hat{\alpha}_{11}^{CN}$, $\hat{\alpha}_{22}^{CN}$, and $\hat{\alpha}_M$, respectively.

3. Governing equations

In this work, the governing equations describing the stability behavior of FG-CNTRC cylindrical shells under temperature rise are established based on the Donnell shell theory with von Kármán-type geometric nonlinearity. The strain field through the shell thickness, measured at a distance z from the mid-surface, is defined as follows [10-12]

$$\begin{bmatrix}\varepsilon_x\\ \varepsilon_y\\ \gamma_{xy}\end{bmatrix} = \begin{bmatrix}\hat{\varepsilon}_x^{\{0\}}\\ \hat{\varepsilon}_y^{\{0\}}\\ \hat{\gamma}_{xy}^{\{0\}}\end{bmatrix} - z\begin{bmatrix}w_{,xx}\\ w_{,yy}\\ 2w_{,xy}\end{bmatrix}. \tag{5}$$

In this formulation, $\hat{\varepsilon}_x^{\{0\}}$ and $\hat{\varepsilon}_y^{\{0\}}$ correspond to the in-plane normal strain components, whereas $\hat{\gamma}_{xy}^{\{0\}}$ denotes the shear strain within the mid-surface of the shell, and

$$\begin{bmatrix}\hat{\varepsilon}_x^{\{0\}}\\ \hat{\varepsilon}_y^{\{0\}}\\ \hat{\gamma}_{xy}^{\{0\}}\end{bmatrix} = \begin{bmatrix}u_{,x} + w_{,x}^2/2\\ -w/R + v_{,y} + w_{,y}^2/2\\ v_{,x} + w_{,x}w_{,y} + u_{,y}\end{bmatrix}. \tag{6}$$

In the present formulation, $u = u(x,\ y)$, $v = v(x,\ y)$, and $w = w(x,\ y)$ represent the displacement fields along the x-, y-, and z-directions, respectively

From Eq. (6), the compatibility condition of strains in the shell can be established in the following form

$$\hat{\varepsilon}_{y,xx}^{\{0\}} - \hat{\gamma}_{xy,xy}^{\{0\}} + \hat{\varepsilon}_{x,yy}^{\{0\}} = w_{,xy}^2 - w_{,xx}w_{,yy} - \frac{1}{R}w_{,xx}. \tag{7}$$

According to Hooke's law, the constitutive relations between stresses and strains for FG-CNTRC cylindrical shells are given by

$$\sigma_x = \hat{Q}_{11}^{*}\varepsilon_x + \hat{Q}_{12}^{*}\varepsilon_y - \hat{\alpha}_{11}^{CNT}\Delta T,$$
$$\sigma_y = \hat{Q}_{12}^{*}\varepsilon_x + \hat{Q}_{22}^{*}\varepsilon_y - \hat{\alpha}_{22}^{CNT}\Delta T, \tag{8}$$
$$\sigma_{xy} = \hat{Q}_{66}^{*}\gamma_{xy}.$$

where

$$\hat{Q}_{11}^{*} = \frac{\hat{E}_{11}^{CNT}}{1-\hat{\nu}_{12}^{CNT}\hat{\nu}_{21}^{CNT}},\ \hat{Q}_{12}^{*} = \frac{\hat{\nu}_{21}^{CNT}\hat{E}_{11}^{CNT}}{1-\hat{\nu}_{12}^{CNT}\hat{\nu}_{21}^{CNT}},$$
$$\hat{Q}_{22}^{*} = \frac{\hat{E}_{22}^{CNT}}{1-\hat{\nu}_{12}^{CNT}\hat{\nu}_{21}^{CNT}},\ \hat{Q}_{66}^{*} = \hat{G}_{12}^{CNT}.$$

The contribution of the stiffeners is incorporated using the smeared stiffener technique, in which the discrete stiffeners are replaced by equivalent continuously distributed stiffnesses over the shell midsurface. The stiffnesses of the longitudinal and circumferential stiffeners are added along the x- and y-directions, respectively, whereas those of the helical stiffeners are transformed into the global shell coordinates through the inclination angle before being smeared over the shell surface. Thus, the equivalent stiffness and thermal resultant terms of the stiffeners are totaled onto those of the shell. The resultant forces and moments of the stiffened shell are expressed in the global shell coordinate system as follows

$$\begin{bmatrix} N_x \\ N_y \\ N_{xy} \\ M_x \\ M_y \\ M_{xy} \end{bmatrix} = \begin{bmatrix} \hat{F}_{11} & \hat{F}_{12} & 0 & \hat{H}_{11} & \hat{H}_{12} & 0 \\ \hat{F}_{12} & \hat{F}_{22} & 0 & \hat{H}_{12} & \hat{H}_{22} & 0 \\ 0 & 0 & \hat{F}_{66} & 0 & 0 & \hat{H}_{66} \\ \hat{H}_{11} & \hat{H}_{12} & 0 & \hat{G}_{11} & \hat{G}_{12} & 0 \\ \hat{H}_{12} & \hat{H}_{22} & 0 & \hat{G}_{12} & \hat{G}_{22} & 0 \\ 0 & 0 & \hat{H}_{66} & 0 & 0 & \hat{G}_{66} \end{bmatrix} \times \begin{bmatrix} \hat{\varepsilon}_x^{\{0\}} \\ \hat{\varepsilon}_y^{\{0\}} \\ \hat{\gamma}_{xy}^{\{0\}} \\ -w_{,xx} \\ -w_{,yy} \\ -2w_{,xy} \end{bmatrix} - \begin{bmatrix} \hat{\Phi}^*_{1x} \\ \hat{\Phi}^*_{1y} \\ 0 \\ \hat{\Phi}^*_{2x} \\ \hat{\Phi}^*_{2y} \\ 0 \end{bmatrix} \Delta T. \tag{9}$$

where

$$\hat{F}_{11} = \hat{F}^{sh}_{11} + \bar{\mu}_{or}\hat{F}^{st}_{11} + 2\bar{\mu}_{sp}\hat{F}^{sp}_{11}\bar{c}^4,$$

$$\hat{F}_{22} = \hat{F}^{sh}_{22} + \bar{\mu}_{or}\hat{F}^{ri}_{22} + 2\bar{\mu}_{sp}\hat{F}^{sp}_{11}\bar{s}^4,$$

$$\hat{F}_{12} = \hat{F}^{sh}_{12} + 2\bar{\mu}_{sp}\hat{F}^{sp}_{11}\bar{s}^2\bar{c}^2, \hat{F}_{66} = \hat{F}^{sh}_{66} + 2\bar{\mu}_{sp}\hat{F}^{sp}_{11}\bar{s}^2\bar{c}^2,$$

$$\hat{H}_{11} = \hat{H}^{sh}_{11} + \bar{\mu}_{or}\hat{H}^{st}_{11} + 2\bar{\mu}_{sp}\hat{H}^{sp}_{11}\bar{c}^4,$$

$$\hat{H}_{22} = \hat{H}^{sh}_{22} + \bar{\mu}_{or}\hat{H}^{ri}_{22} + 2\bar{\mu}_{sp}\hat{H}^{sp}_{11}\bar{s}^4,$$

$$\hat{H}_{12} = \hat{H}^{sh}_{12} + 2\bar{\mu}_{sp}\hat{H}^{sp}_{11}\bar{s}^2\bar{c}^2, \hat{H}_{66} = \hat{H}^{sh}_{66} + 2\bar{\mu}_{sp}\hat{H}^{sp}_{11}\bar{s}^2 c^2,$$

$$\hat{G}_{11} = \hat{G}^{sh}_{11} + \bar{\mu}_{or}\hat{G}^{st}_{11} + 2\bar{\mu}_{sp}\hat{G}^{sp}_{11}\bar{c}^4,$$

$$\hat{G}_{22} = \hat{G}^{sh}_{22} + \bar{\mu}_{or}\hat{G}^{ri}_{22} + 2\bar{\mu}_{sp}\hat{G}^{sp}_{11}\bar{s}^4,$$

$$\hat{G}_{12} = \hat{G}^{sh}_{12} + 2\bar{\mu}_{sp}\hat{G}^{sp}_{11}\bar{s}^2\bar{c}^2, \hat{G}_{66} = \hat{G}^{sh}_{66} + 2\bar{\mu}_{sp}\hat{G}^{sp}_{11}\bar{s}^2\bar{c}^2,$$

$$\hat{\Phi}^*_{1x} = \hat{\Phi}^{*sh}_{1x} + \bar{\mu}_{or}\hat{\Phi}^{*st}_{1x} + 2\bar{\mu}_{sp}\hat{\Phi}^{*sp}_{1x}\left(\bar{c}^6 + \bar{s}^2\bar{c}^2\right),$$

$$\bar{s} = \sin\delta,\ \bar{c} = \cos\delta,$$

$$\hat{\Phi}^*_{2x} = \hat{\Phi}^{*sh}_{2x} + \bar{\mu}_{or}\hat{\Phi}^{*st}_{2x} + 2\bar{\mu}_{sp}\hat{\Phi}^{*sp}_{2x}\left(\bar{c}^6 + \bar{s}^2\bar{c}^2\right),$$

$$\hat{\Phi}^*_{1y} = \hat{\Phi}^{*sh}_{1y} + \bar{\mu}_{or}\hat{\Phi}^{*ri}_{1y} + 2\bar{\mu}_{sp}\hat{\Phi}^{*sp}_{1x}\left(\bar{s}^6 + \bar{s}^2\bar{c}^2\right),$$

$$\hat{\Phi}^*_{2y} = \hat{\Phi}^{*sh}_{2y} + \bar{\mu}_1\hat{\Phi}^{*ri}_{2y} + 2\bar{\mu}_{sp}\hat{\Phi}^{*sp}_{2x}\left(\bar{s}^6 + \bar{s}^2\bar{c}^2\right).$$

where $\bar{\mu}_{or}$ and $\bar{\mu}_{sp}$ are indicator parameters representing the presence of orthogonal and helical stiffeners, respectively. Specifically, $\bar{\mu}_{or} = 1$ and $\bar{\mu}_{sp} = 0$ correspond to the case of orthogonally stiffened shells, whereas $\bar{\mu}_{or} = 0$ and $\bar{\mu}_{sp} = 1$ represent shells reinforced with helical stiffeners. In the absence of stiffeners, both parameters vanish, i.e., $\bar{\mu}_{or} = \bar{\mu}_{sp} = 0$, and

$$\left(\hat{F}^{sh}_{ij}, \hat{H}^{sh}_{ij}, \hat{G}^{sh}_{ij}\right) = \int_{-h/2}^{h/2} \hat{Q}^*_{ij}(z)\left(1, z, z^2\right)dz, \quad (i,j = 1,2,6)$$

$$\left(\hat{\Phi}^{*sh}_{1x}, \hat{\Phi}^{*sh}_{2x}\right) = \int_{-h/2}^{h/2}\left(\hat{Q}^*_{11}\hat{\alpha}^{CNT}_{11} + \hat{Q}^*_{12}\hat{\alpha}^{CNT}_{22}\right)\left(1, z^2\right)dz,$$

$$\left(\hat{\Phi}^{*sh}_{1y}, \hat{\Phi}^{*sh}_{2y}\right) = \int_{-h/2}^{h/2}\left(\hat{Q}^*_{12}\hat{\alpha}^{CNT}_{11} + \hat{Q}^*_{22}\hat{\alpha}^{CNT}_{22}\right)\left(1, z^2\right)dz,$$

$$\left(\hat{\Phi}^{*st}_{1x}, \hat{\Phi}^{*st}_{2x}\right) = \left(\hat{\Phi}^{sp}_{1x}, \hat{\Phi}^{sp}_{2x}\right) = \frac{b_{(st,sp)}}{d_{(st,sp)}}\int_{h/2}^{h/2+h_{(st,sp)}}\left(\hat{Q}^*_{11}\hat{\alpha}^{CNT}_{11} + \hat{Q}^*_{12}\hat{\alpha}^{CNT}_{22}\right)\left(1, z^2\right)dz,$$

$$\left(\hat{\Phi}^{*ri}_{1y}, \hat{\Phi}^{*ri}_{2y}\right) = \frac{b_{ri}}{d_{ri}}\int_{h/2}^{h/2+h_{ri}}\left(\hat{Q}^*_{12}\hat{\alpha}^{CNT}_{11} + \hat{Q}^*_{22}\hat{\alpha}^{CNT}_{22}\right)\left(1, z^2\right)dz.$$

The stiffness contributions of the longitudinal and helical stiffeners, denoted by $\hat{F}^{(st,sp)}_{11}, \hat{H}^{(st,sp)}_{11}$, and $\hat{G}^{(st,sp)}_{11}$ can be expressed as follows

$$\begin{bmatrix} \hat{F}^{(st,sp)}_{11} & \hat{H}^{(st,sp)}_{11} \\ \hat{H}^{(st,sp)}_{11} & \hat{G}^{(st,sp)}_{11} \end{bmatrix} = \begin{bmatrix} \hat{F}^*_{11} & \hat{H}^*_{11} \\ \hat{H}^*_{11} & \hat{G}^*_{11} \end{bmatrix} - \begin{bmatrix} \hat{F}^*_{12} & 0 & \hat{H}^*_{12} & 0 \\ \hat{H}^*_{12} & 0 & \hat{G}^*_{12} & 0 \end{bmatrix} \times \begin{bmatrix} \hat{F}^*_{22} & 0 & \hat{H}^*_{22} & 0 \\ 0 & \hat{F}^*_{66} & 0 & \hat{H}^*_{66} \\ \hat{H}^*_{22} & 0 & \hat{G}^*_{22} & 0 \\ 0 & \hat{H}^*_{66} & 0 & \hat{G}^*_{66} \end{bmatrix}^{-1} \begin{bmatrix} \hat{F}^*_{12} & \hat{H}^*_{12} \\ 0 & 0 \\ \hat{H}^*_{12} & \hat{G}^*_{66} \\ 0 & 0 \end{bmatrix}. \tag{10}$$

where

$$\left(\hat{F}^*_{ij}, \hat{H}^*_{ij}, \hat{G}^*_{ij}\right) = \frac{b_{(st,sp)}}{d_{(st,sp)}}\int_{h/2}^{h/2+h_{(st,sp)}} \hat{Q}^*_{ij}\left(1, z, z^2\right)dz. \tag{11}$$

$$(i,j = 1,2,6)$$

It should be noted that the stiffness terms corresponding to the circumferential stiffeners, namely $\hat{F}^{ri}_{22}, \hat{H}^{ri}_{22}$, and $\hat{G}^{ri}_{22}$, are obtained by exchanging the indices “11” and “22” in Eqs. (10)

and (11). Furthermore, the geometric parameters $b_{(st,sp)}$ and $d_{(st,sp)}$ are substituted by b_{ri} and d_{ri}, respectively.

To satisfy the governing conditions, the Airy stress function $\hat{\varphi}^*(x,y)$ is introduced in the following form

$$N_x = \hat{\varphi}^*_{,yy},\ \ N_y = \hat{\varphi}^*_{,xx},\ \ N_{xy} = -\hat{\varphi}^*_{,xy}. \tag{12}$$

By substituting Eqs. (12), (6) into Eq. (7), the latter can be rewritten in the following form

$$\begin{aligned}&\hat{F}^*_{22}\hat{\varphi}^*_{,xxxx} + \left(\hat{F}^*_{66} + 2\hat{F}^*_{12}\right)\hat{\varphi}^*_{,xxyy} + \hat{F}^*_{11}\hat{\varphi}^*_{,yyyy} + \\ &\hat{H}^*_{21}w_{,xxxx} + \left(\hat{H}^*_{11} + \hat{H}^*_{22} - 2\hat{H}^*_{66}\right)w_{,xxyy} + \\ &\hat{H}^*_{12}w_{,yyyy} - w^2_{,xy} + w_{,xx}w_{,yy} + \frac{1}{R}w_{,xx} = 0.\end{aligned} \tag{13}$$

where

$$\hat{F}^*_{11} = \frac{\hat{F}_{22}}{\hat{F}_{11}\hat{F}_{22} - \hat{F}^2_{12}},\ \hat{F}^*_{22} = \frac{\hat{F}_{11}}{\hat{F}_{11}\hat{F}_{22} - \hat{F}^2_{12}},$$
$$\hat{F}^*_{12} = -\frac{\hat{F}_{12}}{\hat{F}_{11}\hat{F}_{22} - \hat{F}^2_{12}},\ \hat{F}^*_{66} = \frac{1}{\hat{F}_{66}},$$
$$\hat{H}^*_{11} = \hat{F}^*_{11}\hat{H}_{11} + \hat{F}^*_{12}\hat{H}_{12},\ \ \hat{H}^*_{22} = \hat{F}^*_{22}\hat{H}_{22} + \hat{F}^*_{12}\hat{H}_{12},$$
$$\hat{H}^*_{12} = \hat{F}^*_{11}\hat{H}_{12} + \hat{F}^*_{12}\hat{H}_{22},$$
$$\hat{H}^*_{21} = \hat{F}^*_{22}\hat{H}_{12} + \hat{F}^*_{12}\hat{H}_{11},\ \ \hat{H}^*_{66} = \frac{\hat{H}_{66}}{\hat{F}_{66}}.$$

4. Assumed Deflection Function and Solution Procedure

In this study, the FG-CNTRC cylindrical shell is considered to have simply supported and immovable boundary conditions at both ends. Based on these constraints, an approximate analytical form of the deflection function is assumed as follows [11]

$$w = \hat{W}_0 + \hat{W}_1\sin\bar{a}_m x\sin\bar{b}_n y + \hat{W}_2\sin^2\bar{a}_m x \tag{14}$$

where $\bar{a}_m = \dfrac{m\pi}{L};\ \bar{b}_n = \dfrac{n}{R}.$

In the Ritz-based approach, the assumed deflection function approximately satisfies the boundary conditions, and this approximation has been shown in previous studies to have a negligible effect on the predicted buckling and postbuckling responses.

By substituting the assumed deflection function in Eq. (14) into Eq. (13), the corresponding stress function can be obtained as follows

$$\begin{aligned}\hat{\varphi}^* &= \hat{\varphi}^*_1\cos 2\bar{a}_m x + \hat{\varphi}^*_2\cos 2\bar{b}_n y \\ &+\hat{\varphi}^*_3\sin\bar{a}_m x\sin\bar{b}_n y + \hat{\varphi}^*_4\sin 3\bar{a}_m x\sin\bar{b}_n y \\ &-\frac{\sigma_{0y}hx^2}{2} + \frac{N_{0x}y^2}{2}.\end{aligned} \tag{15}$$

where

$$\hat{\varphi}^*_1 = \bar{k}_1\hat{W}_2 + k_2\hat{W}^2_1,$$
$$\hat{\varphi}^*_2 = \bar{k}_3\hat{W}^2_1,$$
$$\hat{\varphi}^*_3 = \bar{k}_4\hat{W}_1\hat{W}_2 + \bar{k}_5\hat{W}_1,$$
$$\hat{\varphi}^*_4 = \bar{k}_6\hat{W}_1\hat{W}_2,$$
$$\bar{k}_1 = \frac{4R\bar{a}^2_m\hat{H}^*_{21} - 1}{8R\bar{a}^2_m\hat{F}^*_{22}},\ \bar{k}_2 = \frac{\bar{b}^2_n}{32\bar{a}^2_m\hat{F}^*_{22}},\ \bar{k}_3 = \frac{\bar{a}^2_m}{32\bar{b}^2_n\hat{F}^*_{11}},$$
$$\bar{k}_4 = -\frac{\bar{b}^2_n\bar{a}^2_m}{\bar{a}^4_m\hat{F}^*_{22} + \bar{a}^2_m\bar{b}^2_n\left(\hat{F}^*_{66} + 2\hat{F}^*_{12}\right) + \bar{b}^4_n\hat{F}^*_{11}},$$
$$\bar{k}_5 = -\frac{\bar{a}^4_m\hat{H}^*_{21} + \bar{a}^2_m\bar{b}^2_n\left(\hat{H}^*_{11} + \hat{H}^*_{22} - 2\hat{H}^*_{66}\right) + \bar{b}^4_n\hat{H}^*_{12} - \dfrac{\bar{a}^2_m}{R}}{\bar{a}^4_m\hat{F}^*_{22} + \bar{a}^2_m\bar{b}^2_n\left(\hat{F}^*_{66} + 2\hat{F}^*_{12}\right) + \bar{b}^4_n\hat{F}^*_{11}},$$
$$\bar{k}_6 = \frac{\bar{b}^2_n\bar{a}^2_m}{81\bar{a}^4_m\hat{F}^*_{22} + 9\bar{b}^2_n\bar{a}^2_m\left(\hat{F}^*_{66} + 2\hat{F}^*_{12}\right) + \bar{b}^4_n\hat{F}^*_{11}}.$$

The closed circumferential condition and immovable edge constraints are expressed as follows

$$\int_0^{2\pi R}\int_0^L v_{,y}dxdy = \int_0^{2\pi R}\int_0^L\left(\hat{\varepsilon}^{\{0\}}_y + \frac{w}{R} - \frac{w^2_{,y}}{2}\right)dxdy = 0 \tag{16}$$

$$\int_0^{2\pi R}\int_0^L u_{,x}dxdy = \int_0^{2\pi R}\int_0^L\left(\hat{\varepsilon}^{\{0\}}_x - \frac{w^2_{,x}}{2}\right)dxdy = 0 \tag{17}$$

After some algebraic manipulations, the expressions for the circumferential stress σ_{0y} and the axial force resultant N_{0x}, as given in Eqs. (16) and (17), can be written as follows

$$\begin{aligned}\sigma_{0y} &= \frac{\hat{F}^*_{12}N_{0x}}{h\hat{F}^*_{22}} + \frac{\hat{W}_2}{2Rh\hat{F}^*_{22}} - \frac{\bar{b}^2_n\hat{W}^2_1}{8h\hat{F}^*_{22}} \\ &+\frac{\hat{W}_0}{Rh\hat{F}^*_{22}} + \frac{\left(\hat{\Phi}^*_{1x}\hat{F}^*_{12} + \hat{\Phi}^*_{1y}\hat{F}^*_{22}\right)\Delta T}{h\hat{F}^*_{22}}.\end{aligned} \tag{18}$$

$$N_{0x} = \frac{\bar{\alpha}_m^2 \hat{W}_1^2}{8\hat{F}_{11}^*} + \frac{\bar{\alpha}_m^2 \hat{W}_2^2}{4\hat{F}_{11}^*} + \left(\frac{-\hat{\Phi}_{1y}^* \hat{F}_{12}^*}{\hat{F}_{11}^*} - \hat{\Phi}_{1x}^* \right)\Delta T + \frac{h\sigma_{0y}\hat{F}_{12}^*}{\hat{F}_{11}^*}. \tag{19}$$

In the present thermal buckling problem, no external mechanical work is considered, and the thermal effect is incorporated through the thermoelastic constitutive relations. Therefore, the total potential energy of the shell can be expressed as follows

$$\bar{\Delta}_{Total} = \bar{\Delta}_{in}. \tag{20}$$

The elastic strain energy of the shell can be expressed as follows

$$\bar{\Delta}_{in} = \frac{1}{2}\int_{-h/2}^{h/2}\int_0^{2\pi R}\int_0^L \begin{pmatrix} \sigma_{xy}\gamma_{xy} + \sigma_x \varepsilon_x + \\ \sigma_y \varepsilon_y - \sigma_x \hat{\alpha}_{11}^{CNT}\Delta T \\ -\sigma_y \hat{\alpha}_{22}^{CNT}\Delta T \end{pmatrix} dxdydz. \tag{21}$$

Applying the Ritz energy method yields the governing equations in the following form

$$\frac{\partial \bar{\Delta}_{Total}}{\partial \hat{W}_0} = 0,\ \frac{\partial \bar{\Delta}_{Total}}{\partial \hat{W}_1} = 0,\ \frac{\partial \bar{\Delta}_{Total}}{\partial \hat{W}_2} = 0. \tag{22}$$

By incorporating Eqs. (18) and (19) into Eq. (22), the latter can be reformulated in the following form

$$\hat{V}_{11}\hat{W}_0 + \hat{V}_{12}\hat{W}_1^2 + \hat{V}_{13}\hat{W}_2 + \hat{V}_{14}\hat{W}_2^2 + \hat{V}_{15}\Delta T = 0 \tag{23}$$

$$\begin{gathered} \hat{V}_{21}\hat{W}_0 + \hat{V}_{22}\hat{W}_1^2 + \hat{V}_{23}\hat{W}_2 \\ + \hat{V}_{24}\hat{W}_2^2 + \hat{V}_{25} + \hat{V}_{26}\Delta T = 0 \end{gathered} \tag{24}$$

$$\begin{gathered} \hat{V}_{31}\hat{W}_0 + \hat{V}_{32}\hat{W}_0\hat{W}_2 + \hat{V}_{33}\hat{W}_2\hat{W}_1^2 \\ + \hat{V}_{34}\hat{W}_1^2 + \hat{V}_{35}\hat{W}_2^3 + \hat{V}_{36}\hat{W}_2^2 + \hat{V}_{37}\hat{W}_2 \\ + \hat{V}_{38}\hat{W}_2\Delta T + \hat{V}_{310}\Delta T = 0. \end{gathered} \tag{25}$$

where

$$\hat{V}_{11} = \frac{2\pi L\hat{F}_{11}^*}{\left(\hat{F}_{11}^*\hat{F}_{22}^* - \hat{F}_{12}^{*2}\right)R},\ \hat{V}_{12} = -\frac{\pi L\left(-\bar{a}_m^2\hat{F}_{12}^* + \bar{b}_n^2\hat{F}_{11}^*\right)}{4\left(\hat{F}_{11}^*\hat{F}_{22}^* - \hat{F}_{12}^{*2}\right)},$$

$$\hat{V}_{13} = \frac{\hat{F}_{11}^*\pi L}{\left(\hat{F}_{11}^*\hat{F}_{22}^* - \hat{F}_{12}^{*2}\right)R},\ \hat{V}_{14} = \frac{\pi L\bar{a}_m^2\hat{F}_{12}^*}{2\left(\hat{F}_{11}^*\hat{F}_{22}^* - \hat{F}_{12}^{*2}\right)},$$

$$\hat{V}_{15} = \frac{2\pi L\left(\hat{\Phi}_{1y}^*\hat{F}_{11}^*\hat{F}_{22}^* - \hat{\Phi}_{1y}^*\hat{F}_{12}^{*2}\right)}{\hat{F}_{11}^*\hat{F}_{22}^* - \hat{F}_{12}^{*2}},$$

$$\hat{V}_{21} = -\frac{\pi L\left(-\bar{a}_m^2\hat{F}_{12}^* + \bar{b}_n^2\hat{F}_{11}^*\right)}{2\left(\hat{F}_{11}^*\hat{F}_{22}^* - \hat{F}_{12}^{*2}\right)},$$

$$\hat{V}_{22} = \frac{32\pi LR}{-\hat{F}_{11}^*\hat{F}_{22}^* + \hat{F}_{12}^{*2}} \times \left[\begin{gathered} \hat{F}_{22}^*\left(-\hat{F}_{11}^*\bar{k}_2^2\hat{F}_{22}^* + \hat{F}_{12}^{*2}\bar{k}_2^2 - \frac{1}{512}\right)\bar{a}_m^4 + \frac{2\hat{F}_{12}^*\bar{a}_m^2\bar{b}_n^2}{512} \\ + \bar{b}_n^4\hat{F}_{11}^*\left(-\bar{k}_3^2\hat{F}_{11}^*\hat{F}_{22}^* + \hat{F}_{12}^{*2}\bar{k}_3^2 - \frac{1}{512}\right) \end{gathered} \right].$$

By solving Eq. (23), the expression for $\hat{W}_0$ is derived as follows

$$\hat{W}_0 = -\frac{\hat{V}_{12}\hat{W}_1^2 + \hat{V}_{13}\hat{W}_2 + \hat{V}_{14}\hat{W}_2^2 + \hat{V}_{15}\Delta T}{\hat{V}_{11}} \tag{26}$$

By substituting Eq. (26) into Eq. (24), the expression for $\hat{W}_1$ can be derived in the following form

$$\hat{W}_1^2 = \bar{T}_{12}\hat{W}_2^2 + \bar{T}_{11}\hat{W}_2 + \bar{T}_{13} + \bar{T}_{14}\Delta T \tag{27}$$

Substitution of Eqs. (26) and (27) into Eq. (25) yields the relationship between ΔT and $\hat{W}_2$ in the following form

$$\Delta T = -\frac{\bar{T}_{21}\hat{W}_2^3 + \bar{T}_{22}\hat{W}_2^2 + \bar{T}_{23}\hat{W}_2 + \bar{T}_{28}}{\bar{T}_{24}\hat{W}_2 + \bar{T}_{26}} \tag{28}$$

where

$$\bar{T}_{11} = -\frac{\hat{V}_{11}\hat{V}_{23} - \hat{V}_{13}\hat{V}_{21}}{\hat{V}_{11}\hat{V}_{22} - \hat{V}_{12}\hat{V}_{21}},$$

$$\bar{T}_{12} = -\frac{\hat{V}_{24}\hat{V}_{11} - \hat{V}_{14}\hat{V}_{21}}{\hat{V}_{11}\hat{V}_{22} - \hat{V}_{12}\hat{V}_{21}},$$

$$\bar{T}_{13} = -\frac{\hat{V}_{25}\hat{V}_{11}}{\hat{V}_{11}\hat{V}_{22} - \hat{V}_{12}\hat{V}_{21}},\ \bar{T}_{14} = -\frac{\hat{V}_{11}\hat{V}_{26} - \hat{V}_{15}\hat{V}_{21}}{\hat{V}_{11}\hat{V}_{22} - \hat{V}_{12}\hat{V}_{21}},$$

$$\bar{T}_{21} = -\frac{\hat{V}_{32}\left(\hat{V}_{12}\bar{T}_{12} + \hat{V}_{14}\right)}{\hat{V}_{11}} + \hat{V}_{33}\bar{T}_{12} + \hat{V}_{35},$$

$$\bar{T}_{22} = -\frac{\hat{V}_{31}\left(\hat{V}_{12}\bar{T}_{12} + \hat{V}_{14}\right)}{\hat{V}_{11}} - \frac{\hat{V}_{32}\left(\hat{V}_{12}\bar{T}_{11} + \hat{V}_{13}\right)}{\hat{V}_{11}} + \hat{V}_{33}\bar{T}_{11} + \hat{V}_{34}\bar{T}_{12} + \hat{V}_{36},$$

$$\bar{T}_{23} = -\frac{\hat{V}_{31}\left(\hat{V}_{12}\bar{T}_{11} + \hat{V}_{13}\right)}{\hat{V}_{11}} - \frac{\hat{V}_{32}\hat{V}_{12}\bar{T}_{13}}{\hat{V}_{11}} + \hat{V}_{33}\bar{T}_{13} + \hat{V}_{34}\bar{T}_{11} + \hat{V}_{37},$$

$$\bar{T}_{24} = -\frac{\hat{V}_{32}\left(\hat{V}_{12}\bar{T}_{14} + \hat{V}_{15}\right)}{\hat{V}_{11}} + \hat{V}_{33}\bar{T}_{14} + \hat{V}_{38},\ \bar{T}_{26} = -\frac{\hat{V}_{31}\left(\hat{V}_{12}\bar{T}_{14} + \hat{V}_{15}\right)}{\hat{V}_{11}} + \hat{V}_{34}\bar{T}_{14} + \hat{V}_{310},$$

$$\bar{T}_{28} = -\frac{\hat{V}_{31}\hat{V}_{12}\bar{T}_{13}}{\hat{V}_{11}} + \hat{V}_{34}\bar{T}_{13}.$$

Based on the bifurcation criterion, the upper buckling load is determined by taking the limit $\hat{W}_2 \to 0$, leading to:

$$\Delta T_{cr} = -\frac{\bar{T}_{28}}{\bar{T}_{26}} \quad (29)$$

Within the numerical framework, the critical buckling temperature ΔT_{cr} is identified as the minimum value of the upper buckling load corresponding to all admissible buckling modes (m,n).

The total deflection amplitude is derived from Eq. (14) and can be expressed as follows

$$W_{max} = \hat{W}_0 + \hat{W}_1 + \hat{W}_2 \quad (30)$$

By substituting Eqs. (26) and (27) into Eq. (30), the total deflection amplitude can be obtained as follows

$$W_{max} = \bar{T}_{31}\hat{W}_2^2 + \bar{T}_{32}\hat{W}_2 + \bar{T}_{35} + \bar{T}_{33}\Delta T + \sqrt{\bar{T}_{12}\hat{W}_2^2 + \bar{T}_{11}\hat{W}_2 + \bar{T}_{14}\Delta T + \bar{T}_{13}}. \quad (31)$$

where

$$\bar{T}_{31} = -\frac{\hat{V}_{12}\bar{T}_{12} + \hat{V}_{14}}{\hat{V}_{11}},\ \bar{T}_{32} = \frac{-\hat{V}_{12}\bar{T}_{11} - \hat{V}_{13}}{\hat{V}_{11}} + 1,$$

$$\bar{T}_{33} = -\frac{\hat{V}_{12}\bar{T}_{14} + \hat{V}_{15}}{\hat{V}_{11}},\quad \bar{T}_{35} = -\frac{\hat{V}_{12}\bar{T}_{13}}{\hat{V}_{11}}.$$

5. Numerical examples and discussions

Table 1 is presented to validate the proposed formulation by comparing the predicted critical thermal buckling temperatures of unstiffened FG-CNTRC cylindrical shells with the results reported by Shen [24] and by Hieu and Tung [25]. For both distribution patterns, UD and FG-X, the present results are in close agreement with the reference data, confirming the reliability of the developed approach.

Table 1. Validation of the present formulation through comparison of critical thermal buckling temperatures $T_{cr} = T_0 + \Delta T_{cr}$ (K) for unstiffened FG-CNTRC cylindrical shells with $R/h = 100$, h =1mm, and V^*_{CNT} =0.17

L^2/Rh	Reference	UD	FG-X
100	Shen [24]	383.9038 (1;7)*	397.2143 (1;7)
	Hieu and Tung [25]	379.2385 (1;7)	390.6587 (1;7)
	Present	379.1897 (1;7)	389.1460 (1;3)
300	Shen [24]	387.6421 (1;6)	394.7082 (1;6)
	Hieu and Tung [25]	385.5992 (1;6)	392.1993 (1;6)
	Present	385.5237 (1;6)	391.0371 (1;6)

* The buckling modes $(m;n)$.

In this paper, the comparison between orthogonal and helical stiffeners is conducted under equivalent geometric conditions, with the same stiffener cross-sectional area, material distribution, and spacing, leading to an equivalent amount of added stiffener material. All material parameters of the CNTs and PMMA matrix used for the numerical calculations are adopted from previously published studies [13-15].

Table 2 presents the critical thermal buckling temperatures of FG-CNTRC cylindrical shells for three CNT distribution patterns, namely UD/UD, X/X, and O/O, under three structural configurations: unstiffened shells, shells reinforced by orthogonal stiffeners, and shells reinforced by helical stiffeners. The results are reported for both temperature-dependent (T-D) and temperature-independent (T-ID) material properties. For all CNT distribution patterns, the unstiffened shell gives the lowest critical temperature, the orthogonally stiffened shell provides an intermediate value, and the helically stiffened shell yields the highest buckling resistance. These results demonstrate that helical stiffeners are substantially more effective than orthogonal stiffeners in improving thermal stability. Among the three CNT distribution patterns, the X/X configuration consistently produces the highest critical buckling temperature, whereas the O/O configuration gives the lowest one, for all stiffener arrangements and for both T-D and T-ID cases. This indicates that the X/X distribution provides the most favorable stiffness enhancement against thermal instability, while the O/O pattern is less efficient in resisting thermally induced buckling. The UD/UD configuration always lies between these two extremes. Another important observation is that the critical buckling temperatures predicted with T-ID properties are always higher than those obtained with T-D properties. This difference confirms that material degradation caused by temperature dependence reduces the thermal buckling resistance of the shell-stiffener system. The discrepancy is especially noticeable in the helically stiffened cases. Therefore, neglecting temperature-dependent material properties may lead to an overestimation of the thermal stability of stiffened FG-CNTRC cylindrical shells. Table 2 also shows that the buckling modes change significantly with the stiffener configuration. For unstiffened and orthogonally stiffened shells, the buckling mode is represented by the conventional pair $(m;n)$, whereas for helically stiffened shells the mode is additionally associated with the number of helical stiffeners and the inclination angle, written in the form $(m;n;n_{sp};\delta)$. This indicates that the helical stiffeners not only increase the critical buckling temperature but also modify the instability pattern of the shell in a more complex manner.

Table 2. Critical thermal buckling temperatures ΔT_{cr} (K) of stiffened FG-CNTRC cylindrical shells with different CNT distribution patterns and stiffener configurations (h =2mm, $R = 250h$, $L = 1.5R$, V^*_{CNT} =0.17, $b_{ri} = b_{st} = b_{sp} = h$, $h_{ri} = h_{st} = h_{sp} = 1.5h$, $d_{ri} = d_{st} = d_{sp}$ =75mm, n_{ri} =10, n_{st} =42)

	Stiffener types	T-D	T-ID
UD/UD	Unstiffener	35.83 (2;11)	40.10 (2;11)
	Orthogonal stiffeners	55.81 (3;8)	64.28 (3;8)
	Helical stiffeners	120.78 (6;6;20;61.48)**	153.84 (6;6;20;61.48)
X/X	Unstiffener	39.59 (2;10)	44.83 (2;10)
	Orthogonal stiffeners	64.08 (2;6)	72.60 (2;6)
	Helical stiffeners	141.96 (6;5;22;58.32)	187.92 (6;5;22;58.32)
O/O	Unstiffener	30.90 (3;12)	33.74 (3;12)
	Orthogonal stiffeners	49.36 (3;8)	55.99 (3;8)
	Helical stiffeners	93.39 (8;5;17;66.06)	111.22 (8;5;17;66.06)

** The buckling modes $(m;n;n_{sp};\delta)$

Table 3 presents the critical thermal buckling temperatures of FG-CNTRC cylindrical shells reinforced by helical stiffeners for three CNT distribution patterns, namely UD/UD, X/X, and

O/O, at three CNT volume fractions V^*_{CNT} =0.12, 0.17, 0.28. A clear trend can be observed from the table: for all distribution patterns, the critical buckling temperature reaches its maximum at the intermediate CNT volume fraction V^*_{CNT} =0.17, while lower values are obtained at V^*_{CNT} =0.12 and 0.28. These results indicate that increasing the CNT content does not monotonically improve the thermal buckling resistance, and that an intermediate CNT volume fraction may provide the most favorable thermo-mechanical balance for the present shell-stiffener system. Another important observation is that the X/X distribution consistently provides the highest critical buckling temperature for all CNT volume fractions, whereas the O/O distribution gives the lowest values. With regard to the buckling mode, the values listed in the form $(m;n;n_{sp};\delta)$ show that the instability pattern is also influenced by the CNT distribution. For the UD/UD configuration, the mode remains unchanged as (6;6;20;61.48) for all three CNT volume fractions. For the X/X and O/O distributions, slight changes in the axial and circumferential wave numbers are observed when V^*_{CNT} increases to 0.28, indicating that the CNT grading pattern affects not only the magnitude of the critical temperature but also the preferred buckling mode.

Table 3. Critical thermal buckling temperatures ΔT_{cr} (K) of helically stiffened FG-CNTRC cylindrical shells for different CNT distribution patterns and CNT volume fractions (h =2mm, $R = 250h$, $L = 1.5R$, $b_{sp} = h$, $h_{sp} = 1.5h$, d_{sp} =75mm)

	V^*_{CNT}	T-D	T-ID
UD/UD	0.12	116.11 (6;6;20;61.48)	145.76 (6;6;20;61.48)
	0.17	120.78 (6;6;20;61.48)	153.84 (6;6;20;61.48)
	0.28	113.57 (6;6;20;61.48)	142.59 (6;6;20;61.48)
X/X	0.12	136.35 (6;5;22;58.32)	177.11 (6;5;22;58.32)
	0.17	141.96 (6;5;22;58.32)	187.92 (6;5;22;58.32)
	0.28	133.30 (5;6;22;58.32)	174.24 (5;6;22;58.32)
O/O	0.12	90.04 (8;5;17;66.06)	105.91 (8;5;17;66.06)
	0.17	93.39 (8;5;17;66.06)	111.22 (8;5;17;66.06)
	0.28	88.45 (7;7;17;66.06)	104.88 (7;7;17;66.06)

Table 4 presents the critical thermal buckling temperatures of FG-CNTRC cylindrical shells reinforced by helical stiffeners for three stiffener spacings, d_{sp} =70, 75, and 80 mm, with V^*_{CNT} =0.28. The results are reported for three CNT distribution patterns, UD/UD, X/X, and O/O, under both temperature-dependent (T-D) and temperature-independent (T-ID) material properties. A clear tendency can be observed from the table: increasing the helical stiffener spacing leads to a reduction in the critical thermal buckling temperature for all CNT distribution patterns and for both material models. From a physical viewpoint, this trend is reasonable because reducing d_{sp} increases the number of helical stiffeners distributed over the shell surface, thereby providing greater equivalent stiffness through the smeared stiffener effect. As a result, the shell becomes more resistant to thermally induced instability. The buckling modes listed in the form $(m;n;n_{sp};\delta)$ also show that the instability pattern is affected by the stiffener spacing. As d_{sp} increases, the number of helical stiffeners n_{sp} decreases and the inclination angle δ changes slightly, indicating that the geometric layout of the helical stiffeners influences not only the magnitude of the critical temperature but also the preferred buckling mode.

Fig. 2 illustrates the effects of stiffener configuration, CNT distribution pattern, temperature dependence of material properties, and CNT volume fraction on the postbuckling behavior of FG-CNTRC cylindrical shells. In all subfigures, the postbuckling response is expressed through the relationship between the temperature rise ΔT and the maximum deflection W_{max}/h. In Fig. 2(a), the influence of stiffener type is clearly demonstrated for the X/X distribution under temperature-dependent properties. The unstiffened shell gives the lowest postbuckling path, while the shell reinforced by orthogonal stiffeners shows a moderate increase in the temperature level. The shell with helical stiffeners exhibits by far the highest equilibrium curve, indicating a much stronger resistance to thermally induced buckling and postbuckling deformation. Fig. 2(b) shows the effects of CNT distribution patterns for helically stiffened shells with V^*_{CNT} =0.17. It can be seen that the X/X distribution yields the highest postbuckling path, followed by the UD/UD pattern, whereas the O/O distribution gives the lowest equilibrium temperatures over the entire deflection range. This trend indicates that the X/X grading pattern offers the most favorable stiffness distribution for resisting thermal instability, while the O/O pattern is less effective. The role of temperature dependence is highlighted in Fig. 2(c), where the postbuckling curves obtained with temperature-independent (T-ID) and temperature-dependent (T-D) material properties are compared for the O/O configuration. The T-ID curve lies entirely above the T-D curve, meaning that the temperature-independent model predicts higher buckling and postbuckling temperatures. This difference reflects the stiffness degradation of the constituent materials at elevated temperatures when temperature dependence is taken into account. Fig. 2(d) presents the effect of CNT volume fraction for helically stiffened shells with the X/X distribution under temperature-dependent properties. An interesting non-monotonic trend is observed: the shell with V^*_{CNT} =0.17 attains the highest postbuckling path, whereas the shells with V^*_{CNT} =0.12 and 0.28 exhibit lower responses. In particular, the case V^*_{CNT} =0.28 gives the lowest curve among the three considered values.

Table 4. Effect of helical stiffener spacing on the critical thermal buckling temperature ΔT_{cr} (K) of FG-CNTRC cylindrical shells reinforced by helical stiffeners (h =2mm, $R = 250h$, $L = 1.5R$, V^*_{CNT} =0.28, $b_{sp} = h$, $h_{sp} = 1.5h$)

	d_{sp}	T-D	T-ID
UD/UD	70mm	116.02 (6;6;21;62.10)	145.89 (6;6;21;62.10)
	75mm	113.57 (6;6;20;61.48)	142.59 (6;6;20;61.48)
	80mm	111.41 (6;6;19;61.06)	139.62 (6;6;19;61.06)
X/X	70mm	136.36 (5;6;23;59.17)	178.42 (5;6;23;59.17)
	75mm	133.30 (5;6;22;58.32)	174.24 (5;6;22;58.32)
	80mm	130.57 (5;6;21;57.67)	170.42 (5;6;21;57.67)
O/O	70mm	90.75 (8;5;18;66.35)	107.28 (8;5;18;66.35)
	75mm	88.45 (7;7;17;66.06)	104.88 (7;7;17;66.06)
	80mm	86.67 (7;7;16;65.96)	102.49 (7;7;16;65.96)

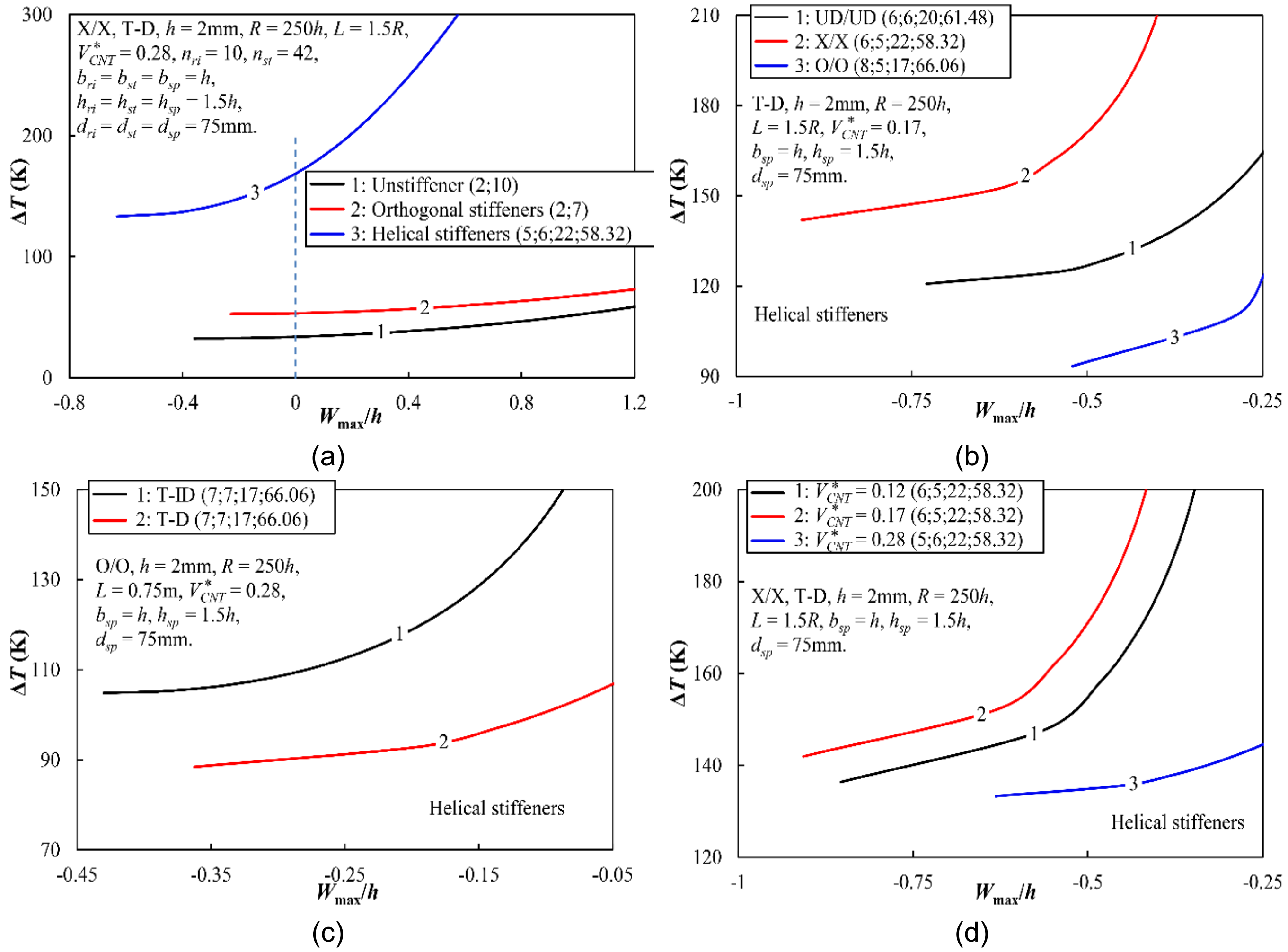

Fig. 2. Effects of stiffener types, CNT distributions, T-ID/T-D properties, and volume fraction of CNT on the postbuckling behavior of shells. (a) Effects of stiffener types; (b) Effects of CNT distributions; (c) Effects of T-ID/T-D properties; (d) Effects of volume fraction of CNT

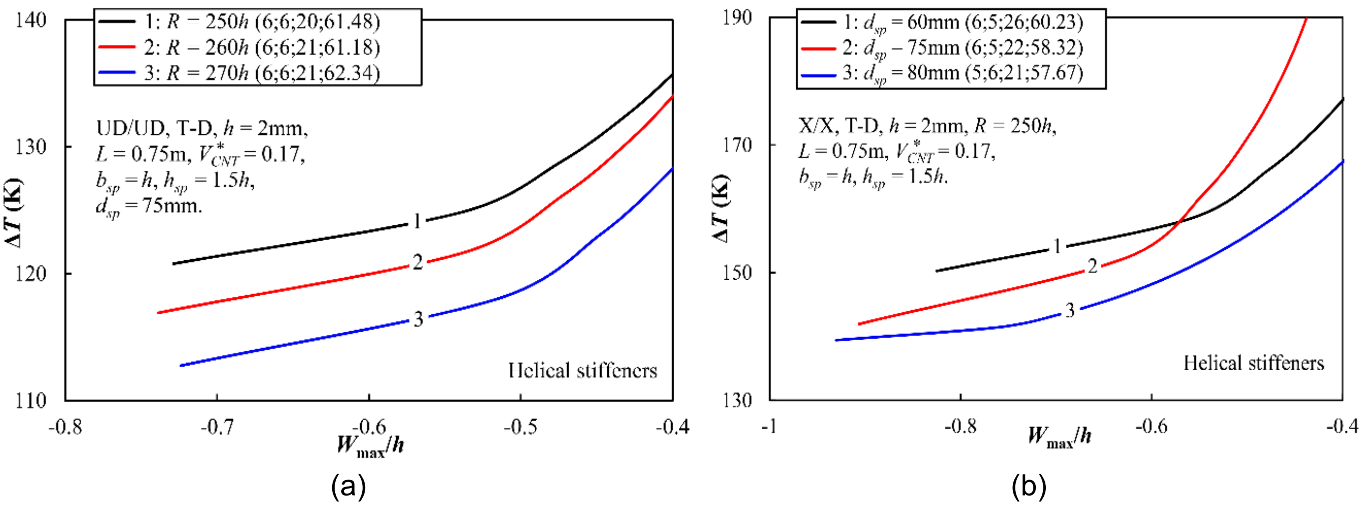

Fig. 3. Effects of radii, stiffener spacings, number of stiffeners, and buckling modes on the postbuckling behavior of shells. (a) Effects of radii; (b) Effects of stiffener spacings; (c) Effects of number of stiffeners; (d) Effects of buckling modes

Fig. 3 illustrates the effects of shell radius, helical stiffener spacing, number of stiffeners, and buckling modes on the postbuckling behavior of FG-CNTRC cylindrical shells reinforced by helical stiffeners. In all four subfigures, the postbuckling response is represented by the relation between the temperature rise ΔT and the normalized maximum deflection W_{max}/h.

Fig. 3(a) shows the influence of the shell radius R for UD/UD shells with helical stiffeners. It can be seen that increasing the radius from $250h$ to $260h$ and then to $270h$ leads to a continuous reduction in the postbuckling path. The shell with $R=250h$ exhibits the highest temperature level, whereas the shell with $R=270h$ gives the lowest one. This trend indicates that larger-radius shells are more susceptible to thermally induced instability.

The effect of helical stiffener spacing is presented in Fig. 3(b) for the X/X distribution. A clear trend is observed: as the stiffener spacing increases from $d_{sp}=60$ mm to 75 mm and 80 mm, the postbuckling curves shift downward.

Fig. 3(c) examines the influence of the number of helical stiffeners n_{sp} for the O/O distribution. The results show that increasing the number of stiffeners from 12 to 15 and 17 significantly raises the postbuckling equilibrium path. In other words, a larger number of helical stiffeners improves the thermal postbuckling resistance of the shell.

Fig. 3(d) highlights the effect of buckling mode for the O/O configuration. Three mode combinations are considered, and the results show that the mode $(m,n)=(7,7)$ yields the lowest postbuckling path, while $(m,n)=(7,10)$ gives the highest one, with $(m,n)=(7,4)$ lying in between. This indicates that the postbuckling response is highly sensitive to the assumed instability mode.

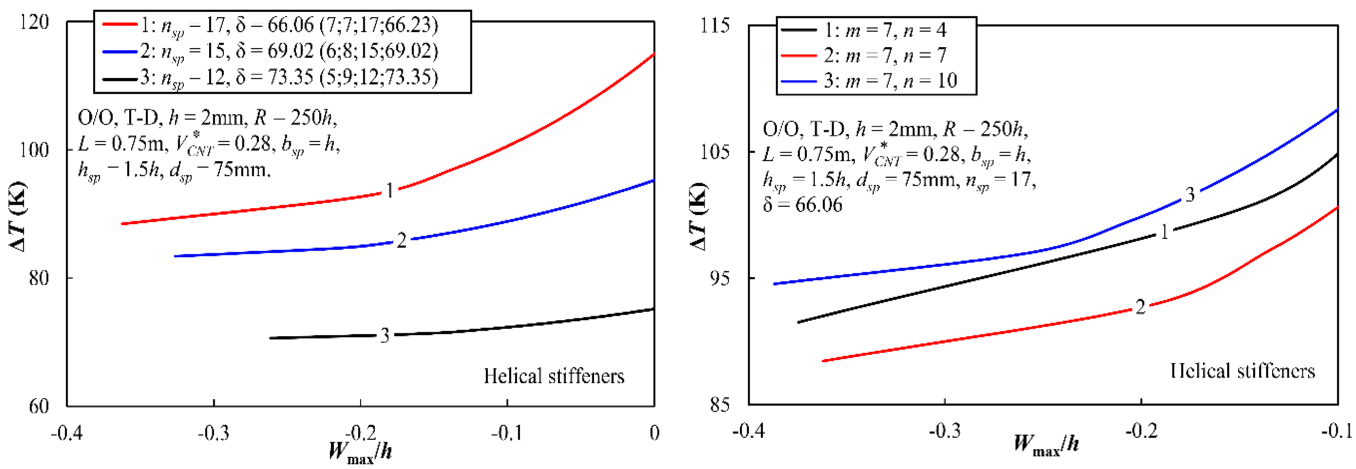

(c) (d)

Fig. 3. (continued)

6. Conclusions

This study presents an analytical investigation into the thermal buckling and postbuckling behavior of FG-CNTRC cylindrical shells reinforced by FG-CNTRC stiffeners under uniform temperature rise. A unified formulation incorporating both orthogonal and helical stiffeners is developed based on the smeared stiffener technique. The governing nonlinear equilibrium equations are established using the Donnell shell theory with von Kármán geometric nonlinearity, and the Ritz energy method is employed to derive analytical expressions for the critical buckling temperature and postbuckling response.

The numerical results demonstrate that the presence of stiffeners significantly enhances the thermal stability of FG-CNTRC cylindrical shells. Among the considered configurations, helical stiffeners provide a substantially greater improvement in both buckling resistance and postbuckling stiffness compared to conventional orthogonal stiffeners.

The influence of CNT distribution patterns is also found to be pronounced. The X/X distribution consistently yields the highest critical buckling temperatures and most favorable postbuckling paths, while the O/O pattern gives the lowest performance, with the UD/UD distribution lying in between.

In addition, the effect of CNT volume fraction exhibits a non-monotonic trend. For the examined cases, $V_{CNT}^{*}=0.17$ gives the highest thermal buckling resistance among the considered CNT volume fractions.

The comparison between temperature-dependent (T-D) and temperature-independent (T-ID) material models reveals that neglecting temperature dependence leads to an overestimation of the critical buckling temperature and postbuckling strength.

Declaration of Generative AI

During the preparation of this work, the authors do not use Generative AI and AI-assisted technologies tools in order to generate the content of the manuscript.

References

[1]. A.H. Sofiyev, E. Schnack. (2004). The stability of functionally graded cylindrical shells under linearly increasing dynamic torsional loading. *Engineering Structures*, 26(10), 1321-1331. https://doi.org/10.1016/j.engstruct.2004.03.016

[2]. A.H. Sofiyev, N. Kuruoglu. (2013). Torsional vibration and buckling of the cylindrical shell with functionally graded coatings surrounded by an elastic medium. *Composites Part B: Engineering*, 45(1), 1133-1142. https://doi.org/10.1016/j.compositesb.2012.09.046

[3]. A.M. Najafov, A.H. Sofiyev, N. Kuruoglu. (2013). Torsional vibration and stability of functionally graded orthotropic cylindrical shells on elastic foundations. *Meccanica*, 48, 829-840. https://doi.org/10.1007/s11012-012-9636-0

[4]. E. Bagherizadeh, Y. Kiani, M.R. Eslami. (2012). Thermal Buckling of Functionally Graded Material Cylindrical Shells on Elastic Foundation. *AIAA Journal*, 50(2), 500-503. https://doi.org/10.2514/1.J051120

[5]. Y. Han, X. Zhu, T. Li, Y. Yu, X. Hu. (2018). Free Vibration and Elastic Critical Load of Functionally Graded Material Thin Cylindrical Shells Under Internal Pressure. *International Journal of Structural Stability and Dynamics*, 18(11), 1850138. https://doi.org/10.1142/S0219455418501389

[6]. Y. Wang, C. Ye, J.W. Zu. (2018). Identifying the temperature effect on the vibrations of functionally graded cylindrical shells with porosities. *Applied Mathematics and Mechanics*, 39(11), 1587-1604. https://doi.org/10.1007/s10483-018-2388-6

[7]. M. Javani, Y. Kiani, M.R. Eslami. (2019). Nonlinear axisymmetric response of temperature-dependent FGM conical shells under rapid heating. *Acta Mechanica*, 230, 3019-3039. https://doi.org/10.1007/s00707-019-02459-y

[8]. K. Xu, Z. Zhou, Q. Lu, J. Sun, Z. Jia. (2019). Thermo-Mechanical Buckling of CFRP Cylindrical Shells with FGPM Coating. *International Journal of Structural Stability and Dynamics*, 19(02), 1950016. https://doi.org/10.1142/S0219455419500160

[9]. M. Arazm, H. Eipakchi, M. Ghannad. (2019). Vibrational behavior investigation of axially functionally graded cylindrical shells under moving pressure. *Acta Mechanica*, 230, 3221-3234. https://doi.org/10.1007/s00707-019-02446-3

[10]. V.H. Nam, N.T. Phuong, K.V. Minh, P.T. Hieu. (2018). Nonlinear thermo-mechanical buckling and post-buckling of multilayer FGM cylindrical shell reinforced by spiral stiffeners surrounded by elastic foundation subjected to torsional loads. *European Journal of Mechanics - A/Solids*, 72, 393-406.

https://doi.org/10.1016/j.euromechsol.2018.06.005

[11]. V.H. Nam, N.T. Phuong, N.T. Trung. (2019). Nonlinear buckling and postbuckling of sandwich FGM cylindrical shells reinforced by spiral stiffeners under torsion loads in thermal environment. *Acta Mechanica*, 230, 3183-3204. https://doi.org/10.1007/s00707-019-02452-5

[12]. N.T. Phuong, D.T. Luan, V.H. Nam, P.T. Hieu. (2019). Nonlinear approach on torsional buckling and postbuckling of functionally graded cylindrical shells reinforced by orthogonal and spiral stiffeners in thermal environment. *Proceedings of the Institution of Mechanical Engineers, Part C: Journal of Mechanical Engineering Science*, 233(6),2091-2106. https://doi.org/10.1177/0954406218780523

[13]. H.S. Shen. (2011). Postbuckling of nanotube-reinforced composite cylindrical shells in thermal environments. Part I: axially-loaded shells. *Composite Structures*, 93(8), 2096-2108. https://doi.org/10.1016/j.compstruct.2011.02.011

[14]. H.S. Shen. (2011). Postbuckling of nanotube-reinforced composite cylindrical shells in thermal environments, Part II: pressure-loaded shells. *Composite Structures*, 93(10), 2496-2503. https://doi.org/10.1016/j.compstruct.2011.04.005

[15]. H.S. Shen. (2014). Torsional postbuckling of nanotube-reinforced composite cylindrical shells in thermal environments. *Composite Structures*, 116, 477-488. https://doi.org/10.1016/j.compstruct.2014.05.039

[16]. Y. Kiani, R. Dimitri, F. Tornabene. (2018). Free vibration of FG-CNT reinforced composite skew cylindrical shells using the Chebyshev-Ritz formulation. *Composites Part B: Engineering*, 147, 169-177. https://doi.org/10.1016/j.compositesb.2018.04.028

[17]. E. Hasrati, R. Ansari, J. Torabi. (2017). Nonlinear forced vibration analysis of FG-CNTRC cylindrical shells under thermal loading using a numerical strategy. *International Journal of Applied Mechanics*, 09(08), 1750108. https://doi.org/10.1142/S1758825117501083

[18]. A.H. Sofiyev, B.E. Turkaslan, R.P. Bayramov, M.U. Salamci. (2019). Analytical solution of stability of FG-CNTRC conical shells under external pressures. *Thin-Walled Structures*, 144, 106338. https://doi.org/10.1016/j.tws.2019.106338

[19]. J.E. Jam, Y. Kiani. (2015). Buckling of pressurized functionally graded carbon nanotube reinforced conical shells. *Composite Structures*, 125, 586-595. https://doi.org/10.1016/j.compstruct.2015.02.052

[20]. L.N. Ly, V.M. Duc, N.T. Trung, N.T. Phuong, D.T. Dong, T.Q. Minh, N.V. Tien, V.T. Hung. (2021). An analytical approach to the nonlinear buckling behavior of axially compressed auxetic-core cylindrical shells with carbon nanotube-reinforced coatings. *Proceedings of the Institution of Mechanical Engineers, Part L: Journal of Materials: Design and Applications*, 235(10), 2254-2265. https://doi.org/10.1177/14644207211033320

[21]. D.T. Dong, V.H. Nam, N.T. Phuong, L.N. Ly, V.M. Duc, N.V. Tien, T.Q. Minh, V.T. Hung, P.H. Quan. (2022). An analytical approach of nonlinear buckling behavior of longitudinally compressed carbon nanotube-reinforced (CNTR) cylindrical shells with CNTR stiffeners in thermal environment. *ZAMM - Journal of Applied Mathematics and Mechanics*, 102(4), e202100228. https://doi.org/10.1002/zamm.202100228

[22]. N.V. Tien, N.T. Phuong, V.M. Duc. T.Q. Minh, D.T. Dong, P.H. Quan, V.H. Nam, L.N. Ly.

(2022). Nonlinear Thermo-Mechanical Buckling of Torsion-Loaded Cylindrical Shells with Eccentric Stiffeners Made from CNT-Reinforced Composite. *Iranian Journal of Science and Technology, Transactions of Mechanical Engineering*, 46, 1107-1119. https://doi.org/10.1007/s40997-021-00482-w

[23]. M.H. Hajmohammad, R. Kolahchi, M.S. Zarei, M. Maleki. (2018). Earthquake induced dynamic deflection of submerged viscoelastic cylindrical shell reinforced by agglomerated CNTs considering thermal and moisture effects. *Composite Structures*, 187, 498-508. https://doi.org/10.1016/j.compstruct.2017.12.004

[24]. H.S. Shen. (2012). Thermal buckling and postbuckling behavior of functionally graded carbon nanotube-reinforced composite cylindrical shells. *Composites Part B: Engineering*, 43(3), 1030-1038. https://doi.org/10.1016/j.compositesb.2011.10.004

[25]. P.T. Hieu, H.V. Tung. (2021). Thermal buckling and postbuckling of CNT-reinforced composite cylindrical shell surrounded by an elastic medium with tangentially restrained edges. *Journal of Thermoplastic Composite Materials*, 34(7), 861-883. https://doi.org/10.1177/0892705719853611